Title

Buried-interface crystallization limits the transferability of high-efficiency perovskite precursor compositions

Journal

Joule

ISSN

2542-4351

Authors

Kim, Jongbeom

Shin, Nahye

Jeon, Chaehoon

et al.

Publication Date

2026-07-01

DOI

10.1016/j.joule.2026.102591

Joule

Article

Buried-interface crystallization limits the transferability of high-efficiency perovskite precursor compositions

Graphical abstract

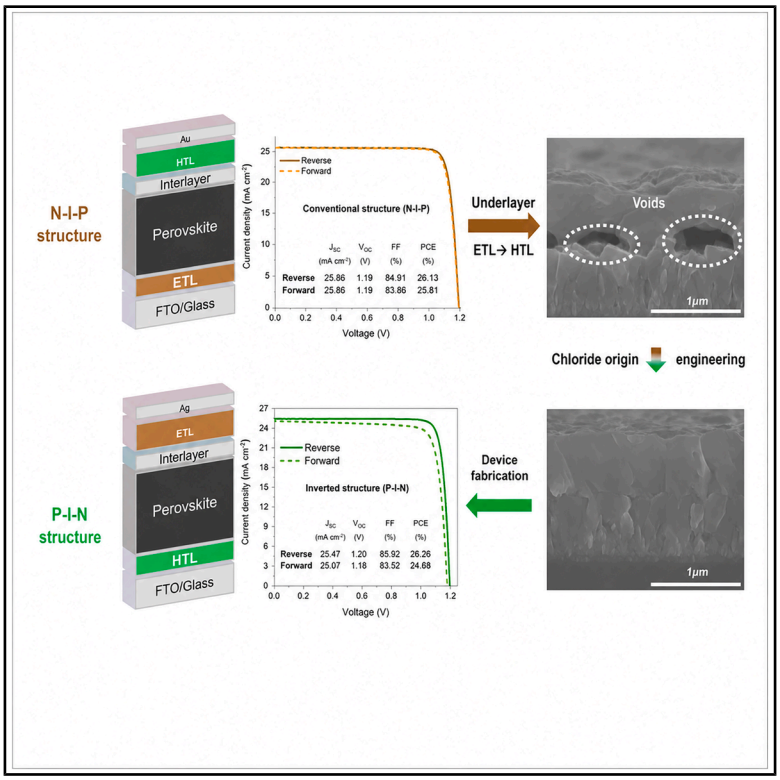

Highlights

- Precursor transferability is limited by buried-interface crystallization
- MACl intermediates persist at hydrophobic SA-HTL interfaces
- $PbCl_2$ coordinates chloride to control interfacial nucleation
- Inverted PSCs reach 26.3% PCE and 86.8% FF with improved stability

Authors

Jongbeom Kim, Nahye Shin, Chaehoon Jeon, ..., Andi Muhammad Risqi, Tae Joo Shin, Sang Il Seok

Correspondence

seoksi@unist.ac.kr

In brief

Perovskite precursor formulations that deliver high efficiencies in conventional n-i-p solar cells often fail to reproduce comparable performance in inverted p-i-n architectures due to the fundamentally different crystallization environment imposed by the underlying layer. Here, we reveal that the underlayer-dependent retention of MACl-derived intermediate phases at the buried interface is responsible for this performance discrepancy. Substituting excess chloride originating from volatile MACl-derived species with $PbCl_2$-derived chloride modulates interfacial nucleation and growth, thereby enabling highly efficient perovskite solar cells.

Kim et al., 2027, Joule *11*, 102591
January 20, 2027
https://doi.org/10.1016/j.joule.2026.102591

CellPress

Joule

CellPress

Article

Buried-interface crystallization limits the transferability of high-efficiency perovskite precursor compositions

Jongbeom Kim,[1,2,5] Nahye Shin,[1,5] Chaehoon Jeon,[1] Seong-hun Lee,[3] Min Jae Paik,[4] Liang Chen,[1] Andi Muhammad Risqi,[1] Tae Joo Shin,[3] and Sang Il Seok[1,6,*]

[1]Department of Energy and Chemical Engineering, Ulsan National Institute of Science and Technology (UNIST), Ulsan 44919, Republic of Korea

[2]Aiiso Yufeng Li Family Department of Chemical and Nano Engineering, University of California, San Diego, La Jolla, CA 92093, USA

[3]Graduate School of Semiconductor Materials and Devices Engineering, Ulsan National Institute of Science and Technology (UNIST), Ulsan 44919, Republic of Korea

[4]Korea Testing & Research Institute, Gwacheon 13810, Gyeonggi-do, Republic of Korea

[5]These authors contributed equally

[6]Lead contact

*Correspondence: seoksi@unist.ac.kr

https://doi.org/10.1016/j.joule.2026.102591

CONTEXT & SCALE Perovskite solar cells (PSCs) have reached high efficiencies in both conventional n-i-p and inverted p-i-n architectures. However, the architecture-dependent nature of perovskite crystallization limits the universal transferability of high-performance precursor formulations. Here, we show that this poor transferability originates from a buried-interface crystallization mismatch, in which methylammonium chloride (MACl)-derived intermediate phases are retained on hydrophobic self-assembled hole-transport layers, inducing interfacial voids and defects. By replacing excess volatile MACl with low-solubility lead chloride ($PbCl_2$), chloride chemistry is localized through Pb–Cl coordination, enabling controlled interfacial nucleation and improving buried-interface quality. This strategy enables inverted PSCs to achieve a power conversion efficiency of 26.3%, fill factors of up to 86.8%, and enhanced stability. These findings provide a practical design principle for adapting high-efficiency perovskite formulations across different device architectures.

SUMMARY

A perovskite precursor solution that delivers power conversion efficiencies (PCEs) exceeding 26% in conventional n-i-p solar cells exhibits severe performance losses when directly applied to inverted p-i-n architectures, revealing that high-efficiency compositions are not inherently transferable. Here, we identify a buried-interface crystallization mismatch, arising from the distinct physicochemical natures of inorganic SnO_2 electron-transporting layers and organic self-assembled hole-transporting monolayers (SA-HTLs), as the origin of this divergence. The methylammonium chloride (MACl)-associated intermediate phase, $MA_2Pb_3I_8 \cdot 2DMSO$, persists and decomposes with strong underlayer dependence, stabilizing beneficially on SnO_2 but impeding crystallization on SA-HTLs. To overcome this limitation, we develop a chloride-origin engineering strategy that decouples chloride functionality from volatile organic ammonium species by incorporating low-solubility lead chloride ($PbCl_2$) with strong Pb–Cl coordination. This enables controlled interfacial desolvation and nucleation on SA-HTLs, suppresses buried defects, and establishes buried-interface crystallization control as a design principle for architecture-convergent, high-efficiency perovskite solar cells.

INTRODUCTION

Perovskite solar cells (PSCs) have advanced rapidly in both conventional n-i-p and inverted p-i-n architectures, with certified power conversion efficiencies (PCEs) in single-junction devices now exceeding 27%.[1–4] These two architectures are fundamentally distinguished by the nature of the charge-transporting underlayer on which perovskite crystallization is initiated. In n-i-p devices, perovskite films are typically deposited on inorganic metal oxide electron transport layers (ETLs), such as

Please cite this article in press as: Kim et al., Buried-interface crystallization limits the transferability of high-efficiency perovskite precursor compositions, Joule (2026), https://doi.org/10.1016/j.joule.2026.102591

SnO_2 or TiO_2, whereas inverted p-i-n devices predominantly rely on organic self-assembled hole-transporting monolayers (SA-HTLs).[5–7] The replacement of TiO_2 with SnO_2 has driven substantial efficiency gains in n-i-p PSCs,[8,9] while in p-i-n architectures, substituting conventional hole-transporting materials such as poly(2,3-dihydrothieno-1,4-dioxin)-poly(styrenesulfonate) (PEDOT:PSS)[10] and poly(triarylamine)[11] with SA-HTL-based contacts has enabled similarly rapid progress.[4,12] These advances arise from the molecular-scale thickness of SA-HTLs, their tunable interfacial dipoles, and their minimal optical and resistive losses.[13,14]

Despite these developments, a persistent performance asymmetry remains between n-i-p and p-i-n architectures when identical perovskite precursor formulations are employed. In our work, SnO_2 ETL-based n-i-p PSCs using formamidinium lead triiodide ($FAPbI_3$)-based absorbers achieved PCEs exceeding 26%.[3,15] However, when the same precursor composition was directly transferred to SA-HTL-based p-i-n devices, a pronounced efficiency loss was observed. This finding challenges a widely held, but rarely scrutinized, assumption in the field: that perovskite precursor compositions optimized for one device architecture are not directly transferable to another.

In high-efficiency $FAPbI_3$-based PSCs, particularly in n-i-p configurations, large amounts of methylammonium chloride (MACl), typically 30–50 mol %,[3,15,16] are routinely incorporated into the precursor solution. MACl is known to retard premature nucleation by forming an intermediate phase with PbI_2, while suppressing the formation of the non-photoactive δ-phase.[17,18] Through the generation of volatile intermediates, MACl lowers the activation energy for the δ-to-α phase transition of $FAPbI_3$, enabling controlled crystallization and improved film morphology.[15,19,20] Consequently, high MACl concentrations have been widely adopted in n-i-p architectures, where perovskite crystallization occurs on high-surface-energy, highly hydrophilic SnO_2 ETLs.[21,22] By contrast, SA-HTLs such as [4-(3,6-dimethyl-9H-carbazol-9-yl)butyl]phosphonic acid (Me-4PACz) in p-i-n architectures exhibit intrinsically low surface energy and hydrophobic surface terminations arising from their long alkyl chains.[23–25] This hydrophobicity increases the contact angle of the perovskite precursor solution and elevates the Gibbs free energy for heterogeneous nucleation (ΔG_{het}), thereby delaying nucleation at the buried interface.[26–28] These considerations underscore the importance of understanding how the contrasting surface properties of inorganic SnO_2 and organic SA-HTLs govern perovskite crystallization from MACl-containing pre cursor solutions.

Here, we elucidate the origin of a buried-interface crystallization mismatch that emerges when identical perovskite precursor solutions containing 30 mol % MACl are processed on inorganic SnO_2 and organic SA-HTL underlayers. We identify the persistence and delayed decomposition of MACl-associated intermediate phases as a primary origin of this mismatch, which becomes particularly detrimental at hydrophobic self-assembled monolayer (SAM) interfaces. By reducing the content of volatile MACl and introducing low-solubility lead chloride ($PbCl_2$), which establishes strong Pb–Cl coordination, we regulate the interfacial desolvation kinetics and nucleation pathway on SAM surfaces. This tailored crystallization control suppresses the formation of buried interfacial defects, facilitates more efficient charge extraction, and markedly reduces non-radiative recombination losses, thereby increasing PCEs.

RESULTS AND DISCUSSION

Architecture-dependent transferability of a perovskite precursor solution

We first examine the transferability of a perovskite precursor solution that delivers high efficiencies in conventional n-i-p devices when applied to inverted p-i-n architectures. As shown in Figure 1A (see Figure S1 and Table S1), n-i-p PSCs employing SnO_2 as the ETL exhibit average PCEs exceeding 25%, with champion devices exceeding 26%, fully consistent with our previous reports.[3,15,22] By sharp contrast, when the identical perovskite precursor composition is applied to p-i-n PSCs based on a SAM + NiO_x hole-transporting layer, the average PCE drops to ∼18%, with a maximum efficiency of only ∼21%. X-ray diffraction (XRD) analysis (Figure S2) reveals that the perovskite films deposited in both architectures exhibit nearly identical crystalline phases, suggesting that bulk phase purity alone cannot account for the pronounced performance disparity. To identify the underlying origin of this efficiency loss, we therefore investigated the perovskite film morphology using both top-view and cross-sectional scanning electron microscopy (SEM). When a precursor containing 30 mol % MACl was deposited on an SnO_2 ETL (denoted as MACl 30 mol %/ETL), the resulting perovskite films exhibited large grain sizes, pinhole-free surfaces, and uniform morphologies, as shown in the top-surface and buried-interface images in Figures 1B and 1C. Cross-sectional SEM images further confirmed a conformal and void-free interface between the perovskite layer and SnO_2 (Figure S3), indicating favorable heterogeneous nucleation and interfacial crystallization on the inorganic underlayer. On the other hand, when the same n-i-p-optimized precursor solution was directly deposited on a Me-4PACz + NiO_x hole-transport layer (denoted as MACl 30 mol %/SA-HTL), pronounced pinholes on the top surface and extensive voids and cracks at the buried interface were observed (Figures 1B and 1C). Cross-sectional imaging reveals large interfacial voids at the perovskite/Me-4PACz interface, which are well known to act as trap-rich non-radiative recombination centers. These interfacial defects lead to severe charge losses, reduced device efficiency, and compromised operational stability. Collectively, these observations demonstrate that a precursor formulation that delivers high efficiency in n-i-p devices fails catastrophically when directly transferred to p-i-n architectures, revealing a fundamental architecture-dependent limitation.

To elucidate the origin of this architecture-dependent failure, we systematically varied the MACl concentration in perovskite films deposited on SA-HTLs. Reducing the MACl content from 30 mol % to 10 mol % (denoted as MACl 10 mol %/SA-HTL) resulted in smaller grain sizes but significantly suppressed pinhole formation at grain boundaries (Figure S4). Correspondingly, PSCs fabricated with MACl 10 mol % exhibited the highest PCE distribution among SA-HTL-based devices (Figure S5), indicating that excessive MACl is detrimental to film formation on hydrophobic SAM underlayers. The structural evolution of these

Please cite this article in press as: Kim et al., Buried-interface crystallization limits the transferability of high-efficiency perovskite precursor compositions, Joule (2026), https://doi.org/10.1016/j.joule.2026.102591

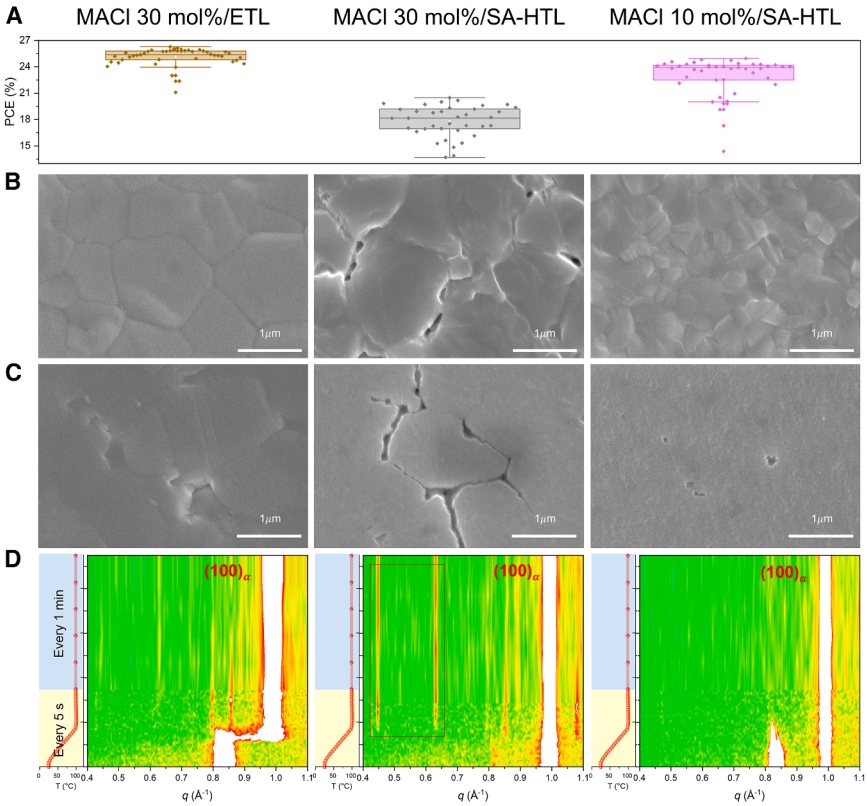

Figure 1. Correlation between film crystallization behavior, interfacial morphology, and photovoltaic performance in MACl-assisted perovskites

(A) Power conversion efficiency (PCE) distributions of the corresponding photovoltaic devices, (B) top-surface SEM images of perovskite thin films prepared with MACl additives of 10 and 30 mol % deposited on ETL SnO_2 and HTL Me-4PACz/NiO_x underlayers, (C) buried-interface SEM images of the corresponding perovskite thin films, (D) *in situ* GI-WAXD intensity maps recorded during film crystallization highlighting differences in crystal orientation evolution.

films during thermal annealing was further investigated by *in situ* grazing-incidence wide-angle XRD (GI-WAXD). For MACl 30 mol %/ETL films (Figure 1D, left), the phase transition from the non-photoactive δ-phase to the photoactive α-phase of $FAPbI_3$ proceeded smoothly upon heating from room temperature (RT) to 100°C. By contrast, MACl 30 mol %/SA-HTL films (Figure 1D, center) exhibited additional diffraction peaks at 0.45 and 0.63 $Å^{-1}$ after several minutes of annealing, corresponding to the (002) and (022) planes of the $MA_2Pb_3I_8 \cdot 2DMSO$ intermediate phase formed through interactions between MA^+ ions and $PbI_2 \cdot$ dimethyl sulfoxide (DMSO) complexes.[5,29] The persistence and delayed decomposition of these volatile intermediate phases, exacerbated by the hydrophobic nature of SAMs, lead to progressive void formation during annealing, as directly observed in Figure S6. By contrast, no distinct intermediate phases are observed in the MACl 10 mol %/SA-HTL system, which preserves a smooth, compact morphology throughout the annealing process (Figure 1D, right). To further clarify the depth-dependent evolution of the intermediate phase, GI-WAXD depth profiling was performed (Figure S7). In the MACl 30 mol % system, a pronounced substrate-dependent difference is observed. For the SA-HTL sample, the intermediate-phase peaks are strongest at larger probing depths at 0 s and remain detectable after 10 s of annealing, indicating preferential retention of the intermediate phase near the buried interface. By contrast, for the SnO_2 sample, the intermediate-phase signal is weaker and disappears much more rapidly, showing no comparable persistence at deeper regions. By 60 s, the intermediate phase is no longer evident in either case. These results demonstrate that under high-MACl conditions, SA-HTL locally stabilizes the intermediate phase near the buried interface, thereby retarding its conversion and delaying crystallization into the perovskite phase. Photovoltaic devices fabricated from these films exhibit performance trends fully consistent with the observed morphological and structural characteristics (Figures 1A and S6; Table S1). While high MACl concentrations are beneficial for promoting perovskite crystallization on inorganic ETLs, inverted p-i-n PSCs based on SA-HTLs require substantially reduced MACl contents to suppress buried-interface defects. Although lowering the MACl concentration effectively mitigates intermediate-phase formation, it simultaneously limits the ability to precisely regulate nucleation kinetics and maintain a stable chloride supply at the buried interface, highlighting an intrinsic trade-off in SA-HTL-based p-i-n PSC processing.

Regulation of buried-interface crystallization

To overcome the inherent trade-off between nucleation control and interface quality associated with volatile MACl, we investigated non-volatile chloride sources, including cesium chloride (CsCl), RbCl, KCl, and $PbCl_2$, to enable more stable control of buried interfaces. As shown in Figure S8, alkali metal chlorides yield only modest improvements, whereas $PbCl_2$ delivers the greatest enhancement in device performance. Consistently, SCLC analysis reveals that $PbCl_2$ produces the lowest trap density among all candidates (Figure S9). Notably, the effects of CsCl, RbCl, and KCl are difficult to interpret exclusively in terms of chloride functionality because the added Cs^+, Rb^+, and K^+ may also influence crystallization and defect passivation. By contrast, $PbCl_2$ provides a cleaner platform to evaluate the role of Cl^-, since Pb^{2+} is already a constituent cation of $FAPbI_3$. Therefore, the superior results obtained with $PbCl_2$ strongly support the view that chloride-mediated interfacial crystallization control is the key mechanism. Accordingly, $PbCl_2$ was selected as the optimal chloride source to regulate buried-interface crystallization[30,31] while avoiding the excessive nucleation

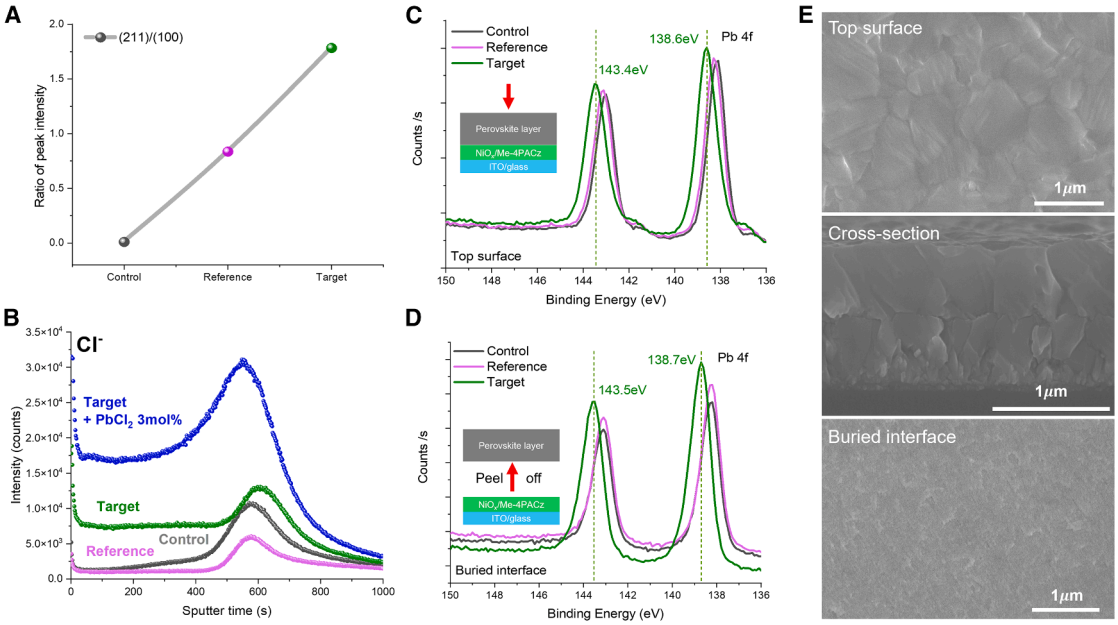

Figure 2. Crystallographic orientation, chloride distribution, and interfacial chemical states of the target perovskite thin film

(A) Ratio of the XRD peak intensities corresponding to the (100) and (211) reflections; (B) comparison of Cl^- peak intensities obtained from TOF-SIMS analysis; Pb 4f XPS spectra of the perovskite thin film measured at the (C) top surface and (D) buried interface; and (E) top-surface, cross-sectional, and buried-interface views of the target thin film with the stack perovskite/Me-4PACz/NiO_x/FTO/glass.

suppression induced by MACl. Consistently, device performance shows a strong dependence on $PbCl_2$ content, with an optimal condition at 2 mol %, while higher concentrations lead to performance degradation (Figure S10). For clarity, perovskite precursor solutions containing 30 mol % MACl are denoted as control, those with 10 mol % MACl as reference, and those incorporating mixed chloride sources (10 mol % MACl and 2 mol % $PbCl_2$) as target. XRD analysis revealed a progressive reduction in the intensity of the (100) reflection from control to reference and target samples, accompanied by a pronounced enhancement of the high-index (211) reflection in the target film (Figure S11). Consequently, the intensity ratio of the (211)/(100) planes reached its maximum value for the target sample (Figure 2A), indicating a crystallographic orientation shift toward low-surface-energy, high-index facets such as (211).[32–34] Importantly, XRD measurements performed on both bare fluorine-doped tin oxide (FTO) and SA-HTL substrates showed that although precursor-dependent orientation differences were already evident in the bulk films, the enhancement of the (211) peak became much more pronounced on SAM-based substrates, highlighting a significant interfacial contribution to the orientation evolution. To determine whether this orientation evolution occurs during film formation, we further performed time-dependent XRD measurements during the early stage of annealing (Figure S12). While the control film exhibited increasingly dominant α-$FAPbI_3$ growth along the (100) direction, the target film showed a progressive increase in the high-index (211) reflection near ~35° with increasing annealing time. These results indicate that $PbCl_2$-derived nucleation actively participates in the early evolution of crystallographic orientation, rather than merely influencing the structure of the fully annealed film.

This behavior reflects the distinct crystallization roles of $PbCl_2$ depending on its chemical source. MACl-derived chloride, homogeneously distributed in the precursor solution, primarily retards nucleation and stabilizes growth along the thermodynamically favored (100) plane.[16,35] By contrast, $PbCl_2$-derived chloride is likely to remain locally near the buried interface because of its lower solubility and stronger Pb–Cl coordination. This localized chloride can promote desolvation and heterogeneous nucleation at the interface, thereby facilitating the development of the (211)-oriented structure. Contact-angle measurements further supported improved precursor wettability, with the target film showing a smaller contact angle (23.8°) than the control (33.1°) and reference (29.2°) samples (Figure S13). This enhanced wettability is expected to promote more uniform film formation and suppress defect generation at the buried interface. Consistent with these findings, the target films exhibited large, well-connected grains and smooth, void-free morphologies after annealing (Figure S14).

The spatial distribution of chloride after film formation was examined by time-of-flight secondary ion mass spectrometry (TOF-SIMS) (Figures 2B and S15). In the target films, chloride was strongly enriched at both the top surface and the buried interface, while the bulk region showed markedly reduced chloride intensity. Notably, the target + $PbCl_2$ (3 mol %) sample showed even stronger Cl signals at both interfaces, indicating that chloride retention was further enhanced with increasing $PbCl_2$ content. By contrast, films containing only MACl retained little residual chloride after annealing, despite their higher nominal chloride content. Moreover, the pronounced Cl_2^- signal observed in the $PbCl_2$-containing samples suggests the existence of clustered or coordinated Pb–Cl species rather than

Please cite this article in press as: Kim et al., Buried-interface crystallization limits the transferability of high-efficiency perovskite precursor compositions, Joule (2026), https://doi.org/10.1016/j.joule.2026.102591

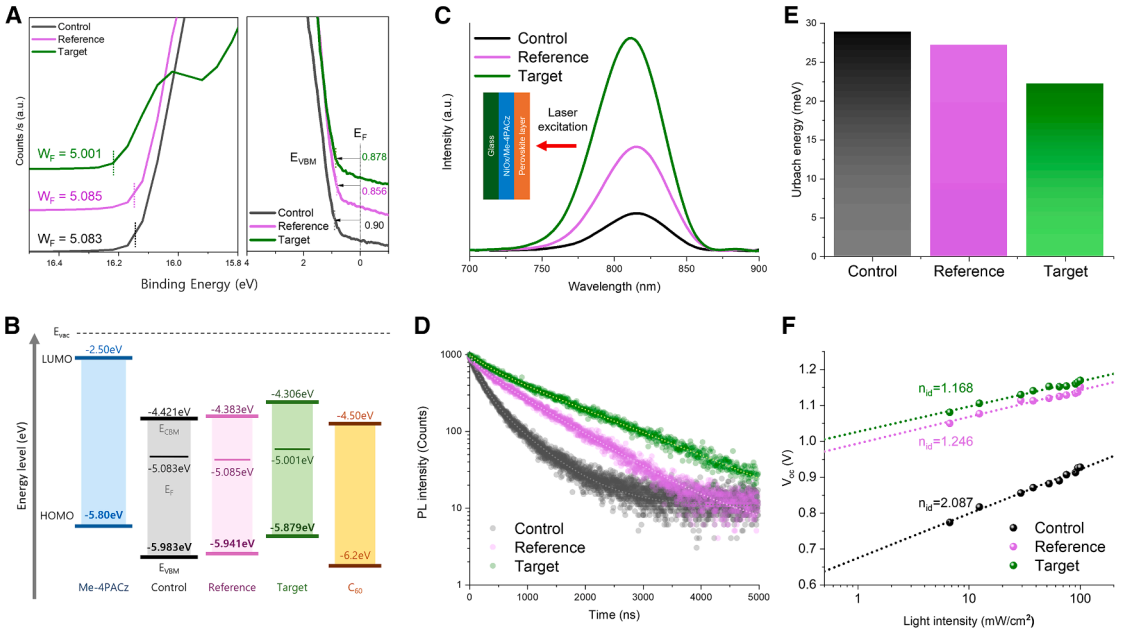

Figure 3. Electronic structure, radiative recombination, energetic disorder, and interfacial charge-recombination characteristics of the perovskite films

(A) UPS spectra of perovskite thin films, (B) energy level scheme of the perovskite films derived from UPS spectra, including the secondary electron cut off and valence band region, (C) steady-state photoluminescence (PL) spectra, (D) time-resolved photoluminescence (TRPL) decay curves measured on Me-4PACz substrates, (E) Urbach energy extracted from absorption spectra, and (F) light-intensity-dependent open-circuit voltage V_{OC} characteristics.

isolated chloride ions. Consistent with this interpretation, excess PbI_2 led to negligible improvement, indicating that Pb^{2+} alone is insufficient and that the observed effects are specifically associated with Pb–Cl chemistry (Figure S16). Overall, these results can be attributed to the much higher volatility of MACl-derived chloride and the stronger retention of Pb-derived chloride during thermal processing. This origin-dependent behavior is attributed to the much higher volatility of MACl-derived chloride and the stronger retention of Pb-derived chloride during annealing. Such a difference can be rationalized by the distinct cation properties: MA^+ carries a +1 charge with a relatively large ionic radius (2.06 Å), whereas Pb^{2+} has a +2 charge and a smaller ionic radius (1.19 Å), resulting in stronger electrostatic attraction between Pb^{2+} and Cl^-.[36] Consistently, UV-vis absorption spectra revealed nearly identical band gaps for the control (1.562 eV) and reference (1.558 eV) samples, whereas the target film exhibited a widened band gap of 1.573 eV (Figure S17), suggesting partial lattice incorporation of Pb–Cl-containing PbX_6 octahedra.

X-Ray photoelectron spectroscopy (XPS) further corroborated this interpretation. High-resolution Pb 4f spectra acquired from both the top surface and buried interface exhibited systematic shifts toward higher binding energies in the target sample compared with the control and reference samples (Figures 2C and 2D), reflecting reduced local electron density around Pb^{2+} due to Pb–Cl coordination.[37] Notably, this shift was more pronounced at the buried interface, consistent with localized chloride action inferred from TOF-SIMS. Complementary shifts in the I 3d core-level spectra (Figure S18) further indicate increased Lewis acidity of Pb induced by Pb–Cl bonding. Cl K-edge X-ray absorption near-edge structure (XANES) analysis shows that the target film exhibits a distinct shift of the Cl K-edge (~2,823 eV) toward lower energy compared with the control and reference (Figure S19A). In Cl K-edge XANES, such a red shift indicates an increase in electron density around the chloride ions or a modification in orbital hybridization due to stronger coordination with the metal center (Pb^{2+}). In addition, the fluorescence intensity profile exhibits a higher signal for the target sample, suggesting a greater amount of residual chloride after film formation (Figure S19B), providing spectroscopic evidence for differences in chloride retention and bonding depending on its origin.[38] Morphological analysis confirmed the complete elimination of pinholes and voids throughout the film thickness and at the buried interface in the target films (Figures 2E and S20). Surface morphology remains largely unchanged with $PbCl_2$, with small particulates appearing only at 5 mol %, while 2 mol % is insufficient to affect the surface, indicating that $PbCl_2$ mainly influences the buried interface (Figure S21). Consistently, on [2-(9H-carbazol-9-yl)ethyl]phosphonic acid (2PACz), the $PbCl_2$-based target improves V_{oc} and fill factor (FF) by suppressing buried interfacial defects, as evidenced by the enhanced J-V characteristics (Figure S22A) and the formation of a uniform, void-free interface (Figure S22B). Efficient charge extraction requires not only defect-free interfaces but also favorable energetic alignment between the perovskite absorber and the charge transport layers.[3,13,14] Ultraviolet photoelectron spectroscopy (UPS) revealed that the target film exhibits a shallower valence band maximum (−5.879 eV)

Please cite this article in press as: Kim et al., Buried-interface crystallization limits the transferability of high-efficiency perovskite precursor compositions, Joule (2026), https://doi.org/10.1016/j.joule.2026.102591

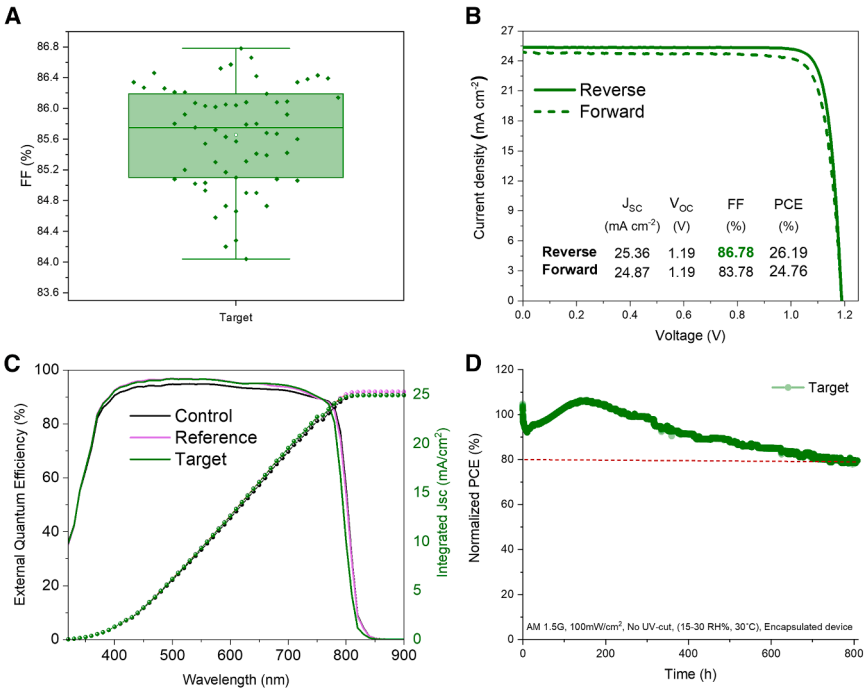

Figure 4. Device statistics and photovoltaic characterization of the target cells with improved FF

(A) Statistical distribution of the fill factor (FF) for the target devices, (B) current density-voltage (J-V) curves of the best-performing target device, highlighting the enhanced FF, measured in reverse and forward scan modes under AM 1.5G illumination, including UV, with an antireflection film, (C) external quantum efficiency (EQE) spectrum of the corresponding device, (D) maximum power point tracking (MPPT) of the target device measured under full AM 1.5G solar illumination (100 mW cm^{-2}) under ambient conditions without a UV filter (Xe lamp).

compared with the control (−5.983 eV) and reference (−5.941 eV) films (Figures 3A and 3B), resulting in a reduced energetic offset between the perovskite valence band and the highest occupied molecular orbital (HOMO) level of Me-4PACz (Figure S23).[39,40]

Steady-state and time-resolved photoluminescence (PL) measurements further demonstrated progressive enhancement of PL intensity and carrier lifetime from control to reference and target samples (Figures 3C and 3D; Table S2), confirming effective suppression of non-radiative recombination.[41] Urbach energy analysis revealed a reduced density of electronic disorder states in the target films (Figures 3E and S24), indicative of enhanced interfacial structural order. The reduction in recombination losses was further reflected in the extracted ideality factor, with the target device exhibiting a notably lower n_{id} (1.168) than the control (2.087) and reference (1.246) devices (Figure 3F),[42,43] consistent with the observed enhancement in FF.

As a direct consequence of resolving buried-interface crystallization mismatch, inverted PSCs fabricated from a precursor originally optimized for n-i-p architectures achieved architecture-convergent high FF. Statistical analysis of 61 devices revealed an average FF of 85.65%, with several devices exceeding 86% (Figure 4A). Additionally, detailed distributions for each parameter responsible for PCE are shown in Figure S25. The best-performing device delivered an FF of 86.78% (J_{SC} = 25.36 mA cm^{-2}, V_{OC} = 1.19 V, PCE = 26.19%) under air mass 1.5 Global (AM 1.5G) illumination (Figure 4B), while the external quantum efficiency (EQE) spectrum yielded an integrated current density of 24.93 mA cm^{-2} (Figure 4C). Additionally, we identified a device that achieved the best PCE of 26.26% in Figure S26. A direct comparison of the J-V characteristics for the control, reference, and target devices is provided in Figure S27. Encapsulated devices exhibited excellent operational stability, retaining approximately 80% of their initial efficiency after 810 h of maximum power point tracking and 97.4% after ~10,000 h under ambient storage conditions (Figures 4D and S28). After prolonged thermal aging, the target maintains a uniform, defect-free buried interface, while the reference exhibits increased interfacial defects, highlighting enhanced FF and improved device stability enabled by $PbCl_2$ (Figure S29).

Conclusions

In summary, this study demonstrates that the limited transferability of high-efficiency perovskite precursor compositions across device architectures stems from a buried-interface crystallization mismatch rather than intrinsic limitations of the perovskite absorber. An identical $FAPbI_3$-based precursor that achieves efficiencies exceeding 26% in SnO_2-based n-i-p devices performs poorly in SA-HTL-based inverted p-i-n architectures due to the fundamentally different surface properties of the underlying layers. We identify the underlayer-dependent persistence of MACl-derived intermediate phases as the primary cause of this mismatch. While MACl enables controlled crystallization on hydrophilic SnO_2, its delayed decomposition on hydrophobic SAMs induces buried interfacial defects and severe recombination losses. By contrast, chloride-origin engineering using low-solubility $PbCl_2$ promotes controlled interfacial nucleation through strong Pb–Cl coordination, effectively suppressing buried defects and enabling inverted devices with a PCE of 26.3% and an FF up to 86.8%.

METHODS

Materials

The following materials were used in the experiments: formamidinium iodide (FAI; 99.99%, Greatcell solar), lead(II) iodide (PbI_2; 99.99%, TCI), glycine hydrochloride (GlyHCl; 99.0%, TCI), lead(II) chloride ($PbCl_2$; 98%, Sigma-Aldrich), CsCl (99.9%, Sigma-Aldrich), rubidium chloride (RbCl; 99.0%, Sigma-Aldrich),

ethanol (EtOH; 99.5%, Sigma-Aldrich), deionized (DI) water (H_2O; Alfa Aesar), N,N-dimethylformamide (DMF; 99.8%, Sigma-Aldrich), DMSO (99.9%, Sigma-Aldrich), 2-propanol (IPA) (99.5%, Sigma-Aldrich), 2-methoxyethanol (2-ME; 99.8%, Sigma-Aldrich), chlorobenzene (99.8%, Sigma-Aldrich), acetonitrile (ACN; 99.8%, Sigma-Aldrich), ethyl ether (99.0%, SAMCHUN), nickel(II) nitrate hexahydrate (97%, Sigma-Aldrich), sodium hydroxide (NaOH, DUKSAN), Me-4PACz (99%, TCI), methylammonium bromide (MABr; 99.99%, Greatcell Solar), lead(II) bromide ($PbBr_2$; 99.998%, Alfa Aesar), cesium iodide (CsI, 99.999%, Sigma-Aldrich), propane-1,3-diammonium iodide ($PDAI_2$; Greatcell Solar), 3-(methylthio)propylamine (3MTPA, 97%, Sigma-Aldrich), C_{60} (99.9%, MS solution), bathocuproine (BCP; purified by sublimation, TCI), propylamine hydrochloride (PACl; Sigma-Aldrich), acetylcholine chloride (ACCl; 99%, Sigma-Aldrich), cyclohexylammonium bromide ((CHA)Br; Greatcell Solar), 4-methoxy-phenethylammonium iodide (MeO-PEAI; 99%, Greatcell Solar), tin(II) chloride dihydrate ($SnCl_2 \cdot 2H_2O$; 98%, Acros), urea (Alfa Aesar), potassium chloride (KCl; 99.999%, Sigma-Aldrich), hydrochloric acid (HCl; 37 wt % in H_2O, Sigma-Aldrich), thioglycolic acid ($C_2H_4O_2S$; 99%, Sigma-Aldrich), 2,2',7,7'-Tetrakis[N,N-di(4-methoxyphenyl)amino]-9,9'-spirobifluorene (spiro-OMeTAD) (Lumtec.), 4-tert-butylpyridine (t-BP; Sigma-Aldrich), bis(trifluoromethane)sulfonimide lithium salt (Li-TFSI; 99.95%, Sigma-Aldrich), and FK209 Co(III) TFSI salt (Lumtec.). All the materials were used as received without any purification.

Synthesis of materials

Formamidinium lead triiodide ($FAPbI_3$) black powder was synthesized by mixing FAI with PbI_2 (1:1 molar ratio) in 11 mL of 2-ME in a 70 mL vial by stirring for 20 min at RT. The mixed solution was heated to 120°C in an oil bath and precipitated using the retrograde method for 1 h. The filtered $FAPbI_3$ powder was then baked at 150°C for 30 min.

For the synthesis of nickel oxide nanoparticles, a 0.5 M solution of nickel(II) nitrate hexahydrate ($Ni(NO_3)_2 \cdot 6H_2O$) was prepared by dissolution in DI water. NaOH was then incrementally added to the solution until a pH of 10 was achieved, under continuous stirring to facilitate the precipitation of $Ni(OH)_2$. Following precipitation, the $Ni(OH)_2$ precipitate was collected by centrifugation and washed twice, first with DI water and then with acetone. Subsequently, acetone was added to create a colloidal solution, which is then dried in a vacuum chamber at 80°C for 2 h. Finally, the dried product was heated in a furnace at 270°C for 2.5 h.

3-(Methylthio)propylamine hydroiodide (3MTPAI) was obtained by the reaction of hydroiodic acid and 3MTPA with a molar ratio of 1:1. Hydroiodic acid was slowly added to the amines under stirring in the ice water bath. The solution was stirred in ice water for 2 h and then rotary evaporated at 50°C until a white solid was obtained, which was washed several times with diethyl ether. Finally, the product was dried in a vacuum-drying oven to obtain the corresponding ammonium halide salts.

Conventional structure device fabrication

FTO glass (Asahi VU glass, 12–13 $\Omega \cdot cm^{-2}$) substrates were sequentially sonicated in acetone, detergent, DI water, and EtOH for 20 min each. The FTO glasses were dipped in a solution prepared by mixing $SnCl_2 \cdot 2H_2O$ (108 mg), urea (500 mg), $C_2H_4O_2S$ (10 μL), and HCl (500 μL) in 40 mL of DI water. The FTO and solution were loaded onto a Hellendahl staining dish in a water chamber at 70°C for 6 h. After the CBD deposition, the SnO_2-deposited FTO substrate was cleaned via sonication with EtOH for 1 min. Then, the FTO/SnO_2 substrate was annealed at 150°C for 1 h, followed by spin-coating with KCl solution (40 mM) in DI water and annealing at 150°C for 15 min. The perovskite precursor solutions were prepared by dissolving 1.42 M $FAPbI_3$ powder with ACCl (0.75 mol %) and MACl (30 mol %) in a mixed solvent of DMF:DMSO = 8:1. The perovskite solutions were then spin-coated onto the substrate at 1,000 rpm for 10 s and 5,000 rpm for 15 s. 1 mL of ethyl ether was dripped onto the substrate during spinning. All perovskite layers were heat-treated at 120°C for 1 h. After cooling, passivation solutions were prepared by mixing 8 mM CHABr and 16 mM MeO-PEAI in IPA. The solutions were spin-coated on the perovskite-coated substrate at 5,000 rpm for 30 s and annealed at 100°C for 5 min. The spiro-OMeTAD solution, prepared by mixing 90 mg mL^{-1} of spiro-OMeTAD in chlorobenzene with 37 μL of t-BP, 23 μL of Li-TFSI salt (516 mg mL^{-1} in ACN), and 9 μL of Co-TFSI salt (375 mg mL^{-1} in ACN), was spin-coated at 3,500 rpm for 30 s. Finally, a 70-nm-thick gold counter electrode was deposited by thermal evaporation.

Inverted structure device fabrication

The washed FTO was treated with oxygen plasma for 20 min. The NiO_x layer was prepared by spin-coating a synthesized NiO_x solution (2 mg/mL) at 4,000 rpm for 30 s on the FTO glass. And then, the substrates were annealed at 120°C for 10 min. After spin-coating a Me-4PACz solution (1 mg/mL) in EtOH at 3,000 rpm for 30 s, the substrate was annealed at 120°C for 5 min. For the perovskite layer deposition, a 1.5 M $(Cs_{0.05}FA_{0.95}PbI_3)_{0.97}(MAPbBr_3)_{0.03}$ precursor solution containing 0.5 mol % GlyHCl, *x* mol % MACl, and *y* mol % $PbCl_2$ (*x* = 10 or 30; *y* = 0 or 2) was prepared by dissolving the corresponding precursors in a mixed solvent of DMF:DMSO = 9:1 (v/v). The precursor solution was transferred into a nitrogen-filled glovebox and spin-coated to deposit the perovskite layer. Spin-coating was performed at 1,000 rpm for 10 s, followed by 6,000 rpm for 20 s. During the second step, 500 μL of ethyl ether was dripped onto the substrate 10 s after the onset of spinning at 6,000 rpm. The perovskite films were then annealed at 110°C for 35 min. Solutions of 3-MTPAI (2 mg mL^{-1}) and $PDAI_2$ (1 mg mL^{-1}) were prepared in a mixed solvent of isopropanol and chlorobenzene (1:1, v/v). The 3-MTPAI solution was first dynamically deposited by spin-coating at 4,500 rpm for 23 s and annealed at 100°C for 5 min, then the same process was repeated for the $PDAI_2$ solution under identical conditions. The as-prepared films were transferred to a thermal evaporation chamber (<10^{-7} torr) for a 25 nm thick C_{60} and 8 nm of BCP deposition. Finally, a 140 nm Ag electrode was deposited on the complete device.

Characterization

The crystal structure was analyzed by using XRD (D/MAX2500V/PC, Rigaku). Steady-state PL and time-resolved PL (TRPL) spectra were measured using a commercial time-correlated

single-photon counting (TCSPC) setup (FluoTime 300, PicoQuant) equipped with a PMA-C-192-M detector and high-resolution excitation monochromators. The J-V characteristics of the devices were measured using a Keithley 2420 source meter under illumination by a solar simulator (Newport, Oriel Sol3A class AAA) with an AM 1.5G filter and 100 mW cm^{-2} irradiation intensity. The active area was determined by placing a metal mask in front of the solar cell to avoid the overestimation of the photocurrent density. A spectral mismatch factor of 1.05 was used for all J-V measurements. For the measurement of high-efficiency devices, an antireflective film (NANOECOWAY) was applied to the surface. EQE was measured using an internal quantum efficiency system (Oriel, IQE 200B) under irradiation by a 100 W xenon (Xe) lamp. The film morphology and thickness were measured using SEM (SU-7000, and SU-8220) operated at 10 kV. Absorbance measurements were performed using an integrating sphere and UV-vis/near-infrared (NIR) spectroscopy (V-780, Jasco). UPS and XPS were conducted using an ESCALAB 250XI instrument (Thermo Fisher Scientific) with a He I (irradiation energy: 21.2 eV) source in a 1×10^{-11} torr vacuum. The electron emitted from the surface can be charged using a flood gun to compensate for the charge on the semiconductor sample. TOF-SIMS profiling measured the depth distributions of Cl^- ions in the perovskite/Me-4PACz/NiO_x on the FTO substrate. The samples were analyzed using a TOF-SIMS V instrument (IONTOF) with a Bi^+ primary beam (25 keV and 1 pA) and Cs^+ sputter beam (0.5 keV and 35 nA). The sputter size was 300×300 μm, the analysis areas were 100×100 μm (for depth profiling) and 500×500 μm (for surface analysis), and the ion area dose was PIDD $6.24e^{+13}$. The hydrophobicity of the perovskite films was measured using contact-angle equipment (DSA100, KRUSS).

GI-WAXD measurements

GI-WAXD measurements were performed at the PLS-II 6D UNIST-PAL beamline at the Pohang Accelerator Laboratory (PAL), Korea. The X-rays from the bending magnet were monochromatized to 18.986 keV (λ = 0.6530 Å) using a double-crystal monochromator focused horizontally and vertically (90 [V] × 120 [H] $μm^2$ full width at half maximum) at the sample position using a sagittal Si(111) crystal and toroidal mirror, respectively. The GI-WAXD sample chamber was equipped with a five-axis motorized stage for fine sample alignment. The 2D GI-WAXD pattern was recorded using a 2D charge-coupled device detector (MX225-HS, Rayonix, USA). The diffraction angles were calibrated using NIST SRM660b (LaB6) with a sample-to-detector distance of 240.7958 mm. An incidence angle of 0.80° was used for the *in situ* GI-WAXD experiments to obtain crystallographic information about the overall thickness of the perovskite films and ensure that all incoming X-rays were irradiated onto the small-length perovskite film sample rather than only passing or being blocked by the substrate or sample stage. The *in situ* GI-WAXD pattern was obtained every 5 s for the initial 3 min and every 1 min between 3 and 20 min, with an X-ray exposure time of 3.5 s. The $FAPbI_3$ film temperature was raised from RT to 100°C in 2 min and maintained at 100°C for 20 min using a fine-tuned temperature controller (Eurotherm 3504 Temperature Controller, Eurotherm, USA).

XANES measurements

Cl K-edge XANES measurements were performed at the 1C (Tender X-ray absorption fine structure [XAFS]) beamline of the PAL, Korea. The X-ray beam was monochromatized to the Cl K-edge (2,822 eV), and spectra were collected in fluorescence mode. The relative chloride content was semi-quantitatively compared using fluorescence signal intensities, assuming uniform film thickness and morphology across the samples.

PL spectra and TRPL analysis

The film was illuminated from the front side using 520 nm excitation. The carrier lifetime values were determined using the bi-exponential equation: $Y = A_1\exp(-t/\tau_1) + A_2\exp(-t/\tau_2)$, where τ_1 and τ_2 represent the fast and slow decay times associated with the trap-assisted non-radiative and radiative recombination processes, respectively. The discrepancies between the PL and carrier lifetimes in the measurement can be attributed to variations in charge transfer to the interlayer rather than to recombination of charges generated in the perovskite.

Device stability test

The stability test at the continuous maximum power point tracking device operation under 1 sun illumination at AM 1.5G (Xe lamp, 450 W) for the encapsulated devices was performed under an inert atmosphere (N_2) by fixing the voltage at V_{MPP} and then tracking the current output.

Ideality factor calculation

$$n_{id} = \frac{q}{k_B T} \frac{d\,(Voc)}{d\,(\ln(I))}, \qquad \text{(Equation 1)}$$

where n_{id} is the ideality factor, k_B is the Boltzmann constant, T is the temperature of the system, q is the charge constant, and I is the normalized light intensity.

UV-vis spectroscopy analysis (Urbach energy)

The UV-vis absorption spectra and Eu of the films were calculated using the equation $\alpha = \alpha_0\exp(h_\nu/E_u)$, where α is the absorption coefficient, and h_ν is the photon energy.

RESOURCE AVAILABILITY

Lead contact

Further information and requests for resources should be directed to and will be fulfilled by the lead contact, Sang Il Seok (seoksi@unist.ac.kr).

Materials availability

This study did not generate any new, unique materials.

Data and code availability

This study did not generate or analyze datasets or code.

ACKNOWLEDGMENTS

This work was supported by the Basic Science Research Program (RS-2018-NR030954) through the National Research Foundation of Korea (NRF) funded by the Ministry of Science, ICT, and Future Planning (MSIP) and the Korea Institute of Energy Technology Evaluation and Planning (KETEP) grant (20213091010010, Super Solar Cells) funded by the Ministry of Trade, Industry

and Energy (MOTIE), Republic of Korea. This study contains the results obtained by using the equipment of UNIST Central Research Facilities (UCRF) and support from the beamline staff at Pohang Accelerator Laboratory (PAL).

AUTHOR CONTRIBUTIONS

J.K., N.S., and S.I.S. conceived the idea and designed the experiments. J.K. and N.S. fabricated inverted PSCs with various electrodes and characterized the films, including data analysis. N.S. and M.J.P. synthesized NiO_x and analyzed defect density. J.K. and C.J. fabricated conventional PSCs. S.-h.L. and T.J.S. measured *ex situ* GI-WAXD. L.C. and A.M.R. analyzed the surface properties of HTL. J.K. led the overall experimental work and wrote the original draft of the manuscript. S.I.S. supervised the project and revised the manuscript. All authors discussed the results and contributed to the final version of the paper.

DECLARATION OF INTERESTS

The authors declare no competing interests.

SUPPLEMENTAL INFORMATION

Supplemental information can be found online at https://doi.org/10.1016/j.joule.2026.102591.

Received: February 2, 2026
Revised: April 23, 2026
Accepted: June 30, 2026

REFERENCES

1. Green, M., Dunlop, E., Yoshita, M., Kopidakis, N., Bothe, K., Siefer, G., Hao, X., and Jiang, J. (2025). Solar Cell Efficiency Tables (Version 66). Prog. Photovolt.: Res. Appl. *33*, 795–810. https://doi.org/10.1002/pip.3919.
2. Cao, F., Bian, L., and Li, L. (2024). Perovskite solar cells with high-efficiency exceeding 25%: A review. Energy Mater. Devices *2*, 9370018. https://doi.org/10.26599/EMD.2024.9370018.
3. Kim, J., Park, J., Lim, J., Kim, J., Kim, J., Shin, N., Yun, J.S., Im, J., and Il Seok, S.I. (2025). Susceptible organic cations enable stable and efficient perovskite solar cells. Joule *9*, 101879. https://doi.org/10.1016/j.joule.2025.101879.
4. Li, G., Zhang, Z., Agyei-Tuffour, B., Wu, L., Gries, T.W., Prashanthan, K., Musiienko, A., Li, J., Zhu, R., and Hart, L.J. (2025). Stabilizing high-efficiency perovskite solar cells via strategic interfacial contact engineering. Nat. Photonics *20*, 55–62.
5. Jeon, N.J., Noh, J.H., Kim, Y.C., Yang, W.S., Ryu, S., and Seok, S.I. (2014). Solvent engineering for high-performance inorganic–organic hybrid perovskite solar cells. Nat. Mater. *13*, 897–903. https://doi.org/10.1038/nmat4014.
6. Yoo, J.J., Seo, G., Chua, M.R., Park, T.G., Lu, Y., Rotermund, F., Kim, Y.-K., Moon, C.S., Jeon, N.J., Correa-Baena, J.-P., et al. (2021). Efficient perovskite solar cells via improved carrier management. Nature *590*, 587–593. https://doi.org/10.1038/s41586-021-03285-w.
7. Lan, Z.-R., Shao, J.-Y., and Zhong, Y.-W. (2023). Self-assembled monolayers as hole-transporting materials for inverted perovskite solar cells. Mol. Syst. Des. Eng. *8*, 1440–1455. https://doi.org/10.1039/d3me00144j.
8. Min, H., Lee, D.Y., Kim, J., Kim, G., Lee, K.S., Kim, J., Paik, M.J., Kim, Y.K., Kim, K.S., Kim, M.G., et al. (2021). Perovskite solar cells with atomically coherent interlayers on SnO2 electrodes. Nature *598*, 444–450. https://doi.org/10.1038/s41586-021-03964-8.
9. Altinkaya, C., Aydin, E., Ugur, E., Isikgor, F.H., Subbiah, A.S., De Bastiani, M., Liu, J., Babayigit, A., Allen, T.G., Laquai, F., et al. (2021). Tin oxide electron-selective layers for efficient, stable, and scalable perovskite solar cells. Adv. Mater. *33*, e2005504. https://doi.org/10.1002/adma.202005504.
10. Jeng, J.Y., Chiang, Y.F., Lee, M.H., Peng, S.R., Guo, T.F., Chen, P., and Wen, T.C. (2013). CH3NH3PbI3 perovskite/fullerene planar-heterojunction hybrid solar cells. Adv. Mater. *25*, 3727–3732. https://doi.org/10.1002/adma.201301327.
11. Luo, D., Yang, W., Wang, Z., Sadhanala, A., Hu, Q., Su, R., Shivanna, R., Trindade, G.F., Watts, J.F., Xu, Z., et al. (2018). Enhanced photovoltage for inverted planar heterojunction perovskite solar cells. Science *360*, 1442–1446. https://doi.org/10.1126/science.aap9282.
12. Tian, C., Sun, A., Chen, J., Zhuang, R., Chen, C., Zheng, J., Liu, S., Du, J., Chen, Q., and Cai, L. (2026). Photostable donor–acceptor interface for minimizing energy loss in inverted perovskite solar cells. Nat. Photonics *20*, 287–295.
13. Tan, Q., Li, Z., Luo, G., Zhang, X., Che, B., Chen, G., Gao, H., He, D., Ma, G., Wang, J., et al. (2023). Inverted perovskite solar cells using dimethylacridine-based dopants. Nature *620*, 545–551. https://doi.org/10.1038/s41586-023-06207-0.
14. Li, Z., Sun, X., Zheng, X., Li, B., Gao, D., Zhang, S., Wu, X., Li, S., Gong, J., Luther, J.M., et al. (2023). Stabilized hole-selective layer for high-performance inverted p-i-n perovskite solar cells. Science *382*, 284–289. https://doi.org/10.1126/science.ade9637.
15. Park, J., Kim, J., Yun, H.-S., Paik, M.J., Noh, E., Mun, H.J., Kim, M.G., Shin, T.J., and Seok, S.I. (2023). Controlled growth of perovskite layers with volatile alkylammonium chlorides. Nature *616*, 724–730. https://doi.org/10.1038/s41586-023-05825-y.
16. Kim, M., Kim, G.-H., Lee, T.K., Choi, I.W., Choi, H.W., Jo, Y., Yoon, Y.J., Kim, J.W., Lee, J., Huh, D., et al. (2019). Methylammonium chloride induces intermediate phase stabilization for efficient perovskite solar cells. Joule *3*, 2179–2192. https://doi.org/10.1016/j.joule.2019.06.014.
17. Fei, C., Guo, L., Li, B., Zhang, R., Fu, H., Tian, J., and Cao, G. (2016). Controlled growth of textured perovskite films towards high performance solar cells. Nano Energy *27*, 17–26. https://doi.org/10.1016/j.nanoen.2016.06.041.
18. Zhang, T., Xu, Q., Xu, F., Fu, Y., Wang, Y., Yan, Y., Zhang, L., and Zhao, Y. (2019). Spontaneous low-temperature crystallization of α-FAPbI3 for highly efficient perovskite solar cells. Sci. Bull. *64*, 1608–1616. https://doi.org/10.1016/j.scib.2019.08.029.
19. Yang, M., Li, Z., Reese, M.O., Reid, O.G., Kim, D.H., Siol, S., Klein, T.R., Yan, Y., Berry, J.J., Van Hest, M.F.A.M., et al. (2017). Perovskite ink with wide processing window for scalable high-efficiency solar cells. Nat. Energy *2*, 1–9. https://doi.org/10.1038/nenergy.2017.38.
20. Bi, L., Fu, Q., Zeng, Z., Wang, Y., Lin, F.R., Cheng, Y., Yip, H.-L., Tsang, S.W., and Jen, A.K.-Y. (2023). Deciphering the roles of MA-based volatile additives for α-FAPbI3 to enable efficient inverted perovskite solar cells. J. Am. Chem. Soc. *145*, 5920–5929. https://doi.org/10.1021/jacs.2c13566.
21. Kim, M., Jeong, J., Lu, H., Lee, T.K., Eickemeyer, F.T., Liu, Y., Choi, I.W., Choi, S.J., Jo, Y., Kim, H.-B., et al. (2022). Conformal quantum dot–SnO2 layers as electron transporters for efficient perovskite solar cells. Science *375*, 302–306. https://doi.org/10.1126/science.abh1885.
22. Paik, M.J., Kim, Y.Y., Kim, J., Park, J., and Seok, S.I. (2024). Ultrafine SnO2 colloids with enhanced interface quality for high-efficiency perovskite solar cells. Joule *8*, 2073–2086. https://doi.org/10.1016/j.joule.2024.04.010.
23. Al-Ashouri, A., Marčinskas, M., Kasparavičius, E., Malinauskas, T., Palmstrom, A., Getautis, V., Albrecht, S., McGehee, M.D., and Magomedov, A. (2023). Wettability improvement of a carbazole-based hole-selective monolayer for reproducible perovskite solar cells. ACS Energy Lett. *8*, 898–900. https://doi.org/10.1021/acsenergylett.2c02629.
24. Al-Ashouri, A., Köhnen, E., Li, B., Magomedov, A., Hempel, H., Caprioglio, P., Márquez, J.A., Morales Vilches, A.B., Kasparavicius, E., Smith, J.A., et al. (2020). Monolithic perovskite/silicon tandem solar cell with >29% efficiency by enhanced hole extraction. Science *370*, 1300–1309. https://doi.org/10.1126/science.abd4016.

25. Pitaro, M., Alonso, J.E.S., Di Mario, L., Romero, D.G., Tran, K., Kardula, J., Zaharia, T., Johansson, M.B., Johansson, E.M.J., Chiechi, R.C., et al. (2024). Tuning the surface energy of hole transport layers based on carbazole self-assembled monolayers for highly efficient Sn/Pb perovskite solar cells. Adv. Funct. Mater. *34*, 2306571. https://doi.org/10.1002/adfm.202306571.

26. Thanh, N.T.K., Maclean, N., and Mahiddine, S. (2014). Mechanisms of nucleation and growth of nanoparticles in solution. Chem. Rev. *114*, 7610–7630. https://doi.org/10.1021/cr400544s.

27. Deng, J., Huang, X., Che, Y., Wang, X., Zhang, X., Wu, B., Yang, L., and Zhang, J. (2024). Salt-Based Catalyzer to Aid Heterogeneous Nucleation Enabling >23% Efficient Electron-Transport-Layer-Free Perovskite Solar Cells. Adv. Funct. Mater. *34*, 2408392. https://doi.org/10.1002/adfm.202408392.

28. LaMer, V.K., and Dinegar, R.H. (1950). Theory, production and mechanism of formation of monodispersed hydrosols. J. Am. Chem. Soc. *72*, 4847–4854. https://doi.org/10.1021/ja01167a001.

29. Petrov, A.A., Fateev, S.A., Khrustalev, V.N., Li, Y., Dorovatovskii, P.V., Zubavichus, Y.V., Goodilin, E.A., and Tarasov, A.B. (2020). Formamidinium haloplumbate intermediates: the missing link in a chain of hybrid perovskites crystallization. Chem. Mater. *32*, 7739–7745. https://doi.org/10.1021/acs.chemmater.0c02156.

30. Pham, N.D., Tiong, V.T., Chen, P., Wang, L., Wilson, G.J., Bell, J., and Wang, H. (2017). Enhanced perovskite electronic properties via a modified lead (ii) chloride Lewis acid–base adduct and their effect in high-efficiency perovskite solar cells. J. Mater. Chem. A *5*, 5195–5203. https://doi.org/10.1039/C6TA11139D.

31. Gao, B., Hu, J., Zuo, Z., Qi, Q., Peng, Z., Chen, H., Yan, K., Hou, S., and Zou, D. (2022). Doping mechanism of perovskite films with PbCl2 prepared by magnetron sputtering for enhanced efficiency of solar cells. ACS Appl. Mater. Interfaces *14*, 40062–40071. https://doi.org/10.1021/acsami.2c11929.

32. Li, S., Xiao, Y., Su, R., Xu, W., Luo, D., Huang, P., Dai, L., Chen, P., Caprioglio, P., Elmestekawy, K.A., et al. (2024). Coherent growth of high-Miller-index facets enhances perovskite solar cells. Nature *635*, 874–881. https://doi.org/10.1038/s41586-024-08159-5.

33. Yang, T., Yang, Y., Niu, T., Zhao, E., Wu, N., Wang, S., Chen, X., Wang, S., Wang, Y., Wu, Y., et al. (2024). Facet Orientation-Dependent Strain Relaxation Stabilizes $FAPbI_3$ Perovskite Solar Cells. ACS Energy Lett. *10*, 427–438. https://doi.org/10.1021/acsenergylett.4c02674.

34. Ghosh, S., and Manna, L. (2018). The many "facets" of halide ions in the chemistry of colloidal inorganic nanocrystals. Chem. Rev. *118*, 7804–7864. https://doi.org/10.1021/acs.chemrev.8b00158.

35. Ma, C., Kang, M.-C., Lee, S.-H., Kwon, S.J., Cha, H.-W., Yang, C.-W., and Park, N.-G. (2022). Photovoltaically top-performing perovskite crystal facets. Joule *6*, 2626–2643. https://doi.org/10.1016/j.joule.2022.09.012.

36. Burger, S., Ehrenreich, M.G., and Kieslich, G. (2018). Tolerance factors of hybrid organic–inorganic perovskites: recent improvements and current state of research. J. Mater. Chem. A *6*, 21785–21793. https://doi.org/10.1039/C8TA05794J.

37. Meggiolaro, D., and De Angelis, F. (2018). First-principles modeling of defects in lead halide perovskites: best practices and open issues. ACS Energy Lett. *3*, 2206–2222. https://doi.org/10.1021/acsenergylett.8b01212.

38. Malta, G., Kondrat, S.A., Freakley, S.J., Morgan, D.J., Gibson, E.K., Wells, P.P., Aramini, M., Gianolio, D., Thompson, P.B.J., Johnston, P., et al. (2020). In situ K-edge X-ray absorption spectroscopy of the ligand environment of single-site Au/C catalysts during acetylene hydrochlorination. Chem. Sci. *11*, 7040–7052. https://doi.org/10.1039/D0SC02152K.

39. Shin, S.S., Park, B.-W., Noh, J.H., and Seok, S.I. (2026). Interlayer engineering in metal halide perovskite photovoltaics. Nat. Photonics *20*, 11–23. https://doi.org/10.1038/s41566-025-01809-8.

40. Yang, W., Ding, B., Lin, Z., Sun, J., Meng, Y., Ding, Y., Sheng, J., Yang, Z., Ye, J., Dyson, P.J., et al. (2023). Visualizing interfacial energy offset and defects in efficient 2D/3D heterojunction perovskite solar cells and modules. Adv. Mater. *35*, e2302071. https://doi.org/10.1002/adma.202302071.

41. Krückemeier, L., Krogmeier, B., Liu, Z., Rau, U., and Kirchartz, T. (2021). Understanding Transient Photoluminescence in Halide Perovskite Layer Stacks and Solar Cells. Adv. Energy Mater. *11*, 2003489. https://doi.org/10.1002/aenm.202003489.

42. Caprioglio, P., Stolterfoht, M., Wolff, C.M., Unold, T., Rech, B., Albrecht, S., and Neher, D. (2019). On the relation between the open-circuit voltage and quasi-Fermi level splitting in efficient perovskite solar cells. Adv. Energy Mater. *9*, 1901631. https://doi.org/10.1002/aenm.201901631.

43. Stolterfoht, M., Grischek, M., Caprioglio, P., Wolff, C.M., Gutierrez-Partida, E., Peña-Camargo, F., Rothhardt, D., Zhang, S., Raoufi, M., Wolansky, J., et al. (2020). How to quantify the efficiency potential of neat perovskite films: Perovskite semiconductors with an implied efficiency exceeding 28%. Adv. Mater. *32*, e2000080. https://doi.org/10.1002/adma.202000080.